Kovove Mater. 62 2024 65–75
DOI: 10.31577/km.2024.2.65

Thermal properties and container compatibility of $(Al_{0.8}Si_{0.2})_{100-x}Bi_x$ phase change energy storage alloys

Lili Sun[1,2], Qing Chang[1], Yongcun Li[1,2,3]*, Xiaodong Wang[1], Jing Tang[1]

[1]*School of Mechanical Science and Engineering, Northeast Petroleum University, 199 Fazhan Road, Daqing 163318, P. R. China*
[2]*Heilongjiang Key Laboratory of Petroleum and Petrochemical Multiphase Treatment and Pollution Prevention, Daqing 163318, Heilongjiang, P. R. China*
[3]*Sanya Offshore Oil&Gas Research Institute, Northeast Petroleum University, Sanya 572025, Hainan, P. R. China*

Received 4 December 2023, received in revised form 29 December 2023, accepted 8 March 2024

Abstract

This study introduces a novel $(Al_{0.8}Si_{0.2})_{100-x}Bi_x$ (x = 1, 2, 3, 4, and 5 at.%) phase change energy storage alloy, showcasing high heat capacity for energy regulation and heat management applications. We investigated the influence of Bi content on the alloy's microstructure, thermal properties, high-temperature stability, and container compatibility using optical microscopy, DSC, XRD, SEM, and EDS. Adding 4 wt.% Bi significantly refines the microstructure, evidenced by reduced eutectic silicon size and increased grain boundaries. The $(Al_{0.8}Si_{0.2})_{96}Bi_4$ alloy achieved a maximum enthalpy change of –397 J g^{-1} and exhibited phase change temperatures of 500–600 °C, suitable for diverse high-temperature applications. The phase composition remained stable after 100 thermal cycles at high temperatures. Static corrosion tests at 560 °C for 240 h revealed enhanced compatibility with SS304 containers, attributed to a dense oxide layer formed by accelerated Cr and Ni atom diffusion through increased grain boundaries. This layer effectively prevents further diffusion of Al and Fe atoms, demonstrating the alloy's improved suitability for practical applications.

K e y w o r d s: Al-Si-Bi alloys, energy storage materials, high-temperature thermal cycling, container compatibility

1. Introduction

Energy storage technology is pivotal in enhancing energy production and consumption and is a cornerstone for developing renewable energy sources. In solar thermal power generation systems, the thermal storage module can reach temperatures of 500–600 ℃; molten salts, commonly used as high-temperature phase change energy storage materials, are hindered by low thermal conductivity and heat capacity [1, 2]. Researchers have shown significant interest in developing energy storage alloys suitable for high-temperature environments in recent years. The Mg-Cu systems [3] and Mg-Al systems are commonly studied [4]. Mg-Cu--based alloys often have relatively small phase change enthalpy, resulting in higher energy consumption in practical applications. Al-Mg-based alloys have a high specific heat capacity and exhibit poor thermal stability. With the recognition of the problems existing in Mg-Cu and Mg-Al alloy systems, finding a type of energy storage alloy with high heat capacity and thermal stability is crucial.

The excellent phase change performance of Al-Si alloys has gradually attracted the attention of researchers. Wang et al. [5, 6] investigated the thermal storage performance and reliability of binary Al-Si phase change alloys and revealed that the alloy exhibits a high phase transition enthalpy of up to 560 J g^{-1}, satisfying the requirements for high-temperature thermal storage modules in solar thermal power generation. In the study conducted by Zhang et al. [7], the effect of Al-Si alloy liquid on the high-temperature corrosion behavior of 310S stainless steel was conducted; it was found that the alloy exhib-

*Corresponding author: tel.: +86 459 6504512; e-mail address: vc_lee1988@163.com

ited significant corrosiveness towards iron-based containers, leading to issues such as leakage during usage. To enhance the application of Al-Si alloys in the field of energy storage, many researchers have focused on alloying approaches to regulate the alloy composition and mitigate the corrosion of container materials. Rawson et al. [2] added Cu element to Al-Si-based alloy and observed that the compatibility with alumina and graphite was better than that of Fe-based metals. Van Ende et al. investigated the influence of oxygen content on the interfacial reaction between Fe and Al [8], and showed that the effective control of the substrate's oxygen content or oxide content can effectively inhibit the permeation of Al atoms. Some studies [9, 10] have also shown that adding a suitable amount of low-melting-point metallic elements of Ga, In, and Bi in the alloy can accelerate the oxidation rate of the substrate without affecting its overall performance. Ga and In have relatively low melting points and are unsuitable for high-temperature environments. Bi is usually used as self-lubricating materials [11, 12] and load--bearing materials; however, there is relatively little research on energy storage applications. The addition of Bi has been observed to alleviate the cracking effect on the matrix, leading to an overall improvement in the mechanical properties of the Al-Si-Bi alloy [13]. Bi exists in a highly dispersed free state within high-silicon aluminum alloys, positively influencing the quantity, distribution, particle size, and roundness of primary silicon [14]. Wei et al. [15] utilized Al-Bi powder as a material for hydrogen production and investigated its thermal and physical properties as a phase change energy storage material. The results demonstrated the commendable reusability and structural stability of Al-Bi powder, positioning it as a potential material for heat storage in concentrated solar power plants. Therefore, adding Bi has varying degrees of favorable impact on Al-Si-based alloys. However, the influence of Bi on the microstructure and properties of Al-Si alloys, as well as their thermal stability and compatibility with different container materials, is in urgent need of systematic research. The corrosion mechanisms in high-temperature environments are all areas that warrant further investigation.

Al-Si-based alloys have emerged as prominent candidates in phase change energy storage materials due to their remarkable thermal properties and high-temperature stability. However, optimizing their microstructural characteristics and container compatibility remains a critical challenge, particularly for high-temperature applications. This article focuses on the strategic incorporation of the Bi element into Al-Si--based alloys to enhance their performance. Specifically, we aim to systematically explore the effects of varying Bi content on the microstructure, thermophysical properties, and high-temperature stability of Al-Si-based phase change energy storage materials. Furthermore, recognizing the importance of material-container interaction, we endeavor to identify the optimal container material and analyze its corrosion resistance mechanism in conjunction with our developed alloys. By addressing these aspects, our study seeks to bridge the existing research gap and contribute to advancing phase change energy storage technologies, particularly in high-temperature applications.

2. Experimental

2.1. Materials preparation

The experiment utilized industrial pure Bi (99.99 %) and an Al-20%Si intermediate alloy. A ceramic crucible was selected, and a ZHF30-3 vacuum tungsten electrode arc furnace was used. The melting temperature was set at 700 ℃, and the heating rate was 20 ℃ min^{-1} using continuous heating. The designed proportions of the Al-20%Si intermediate alloy were added to the crucible. Once the Al-20%Si intermediate alloy was completely melted, Bi powder wrapped in aluminum foil was added. After a 10-minute holding time, a tiny amount of boron was added to improve the mechanical properties [16], and R J-2 refining and covering agents were added to the melt, followed by a 30-minute holding time. The ingots were melted at least four times to ensure chemical homogeneity. All materials were cooled in the furnace. This uniform cooling approach was applied to ensure consistency in the treatment of each specimen. This process produced $(Al_{0.8}Si_{0.2})_{99}Bi_1$, $(Al_{0.8}Si_{0.2})_{98}Bi_2$, $(Al_{0.8}Si_{0.2})_{97}Bi_3$, $(Al_{0.8}Si_{0.2})_{96}Bi_4$, and $(Al_{0.8}Si_{0.2})_{95}Bi_5$ alloys with different Bi contents.

2.2. Measurements of thermophysical properties

The density of samples with different compositions was measured by using Archimedes' method. To ensure the accuracy of the experimental data, three groups of samples at different positions were randomly selected and measured three times, and the average value was taken. Rectangular samples with the size of $20 \times 20 \times 12\,\mathrm{mm}^3$ were first weighed in air (recorded as w_a) and then submerged in water and weighed again (recorded as w_s) at a given temperature. The density of the measured sample (ρ) was determined by $\rho = \rho_\mathrm{w} w_\mathrm{a}/(w_\mathrm{a} - w_\mathrm{s})$, where ρ_w is the density of water. X-ray techniques were not used for porosity evaluation in our samples. Instead, metallurgical examinations of various sections revealed minimal porosity. This suggests a near-zero porosity rate, which is important for assessing material density and integrity.

The microstructures were observed using an optical microscope (Leica DMI 3000, Leica, Germany), en-

Table 1. Chemical composition of container material (wt.%)

Material	C	Si	Mn	Cr	Ni	S	P	Fe
X70	≤ 0.16	≤ 0.45	≤ 1.70	–	–	≤ 0.01	≤ 0.02	Balance
304	≤ 0.08	≤ 1.00	≤ 2.00	18.0–20.0	8.00–10.0	≤ 0.03	≤ 0.045	Balance
2Cr13	0.16–0.25	≤ 1.00	≤ 1.00	12.0–14.0	≤ 0.60	≤ 0.03	≤ 0.040	Balance

suring a representative sample selection by following a randomized sampling method across different batches. The thermal stability was tested using a ZHF30-3 vacuum tungsten electrode arc furnace. Al_2O_3 crucibles were used for the test. The temperature range for the thermal cycling was set from 560 to 620 ℃. This temperature range constituted one thermal cycle repeated for 100 cycles. Differential scanning calorimetry (DSC) analysis was conducted on the extracted samples using a NETZSCH STA 449C instrument to analyze the effects of the number of cycles on the phase transition temperature and latent heat of the energy storage alloy. X-ray diffraction (X'PertPro MRD) analysis was performed to analyze the phase composition after different numbers of cycles. By comprehensively evaluating these results, the thermal stability of the alloy was determined.

2.3 Static crucible reaction experiments

The compatibility between Al80Si20 and $(Al_{0.8}Si_{0.2})_{96}Bi_4$ alloy and container materials was evaluated through the immersion corrosion method. The container materials included SS304 stainless steel ($40 \times 13.1 \times 2\,mm^3$), 2Cr13 steel ($40 \times 13.1 \times 2\,mm^3$) and X70 steel ($4 \times 13.1 \times 2\,mm^3$). The composition and content of the specimen materials are shown in Table 1.

Before the experiment, the SS304 stainless steel, 2Cr13 steel, and X70 steel specimens were subjected to surface cleaning using an ultrasonic cleaning device for 15 min. The cleaned specimens were dried and weighed. The samples were suspended in six different alumina crucibles. Three crucibles were filled with Al80Si20 alloy, while the remaining crucibles were filled with $(Al_{0.8}Si_{0.2})_{96}Bi_4$ alloy. The alumina crucibles were first placed in a vacuum tungsten arc furnace, and the temperature was set to 200 ℃. After reaching the desired temperature, a 10-minute dwell time was applied. The temperature was then raised to 500 ℃ and maintained for 15 min. Finally, the temperature was set to 560 ℃ and held constant. After 24, 72, 144, and 240 h immersion, the suspended samples were individually retrieved and promptly cleaned to remove the surface metal film. The corrosion rate was determined through weight measurement. SEM observations using a Zeiss Ultra-55 Scanning Electron Microscope were carried out.

The calculation formulas of corrosion rate and corrosion layer thickness are shown in Eq. (1) and Eq. (2), respectively:

$$V = \frac{\Delta W}{At}, \tag{1}$$

$$X = \frac{\Delta W}{A\rho}, \tag{2}$$

where V is the corrosion rate ($g\,mm^{-2}\,h^{-1}$), ΔW is the mass change before and after corrosion (g), A is the surface area of the sample (mm^2), X is the thickness of the corrosion layer (mm), ρ is the material density ($g\,mm^{-3}$), and t is the corrosion time (h).

3. Results and discussion

3.1. Microstructure analysis

Figure 1 illustrates the microstructure of $(Al_{0.8}Si_{0.2})_{100-x}Bi_x$ (x = 1, 2, 3, 4, and 5 at.%) alloy. The light-colored region represents the α-Al phase, while the dark-gray region represents the Si crystals formed in the eutectic structure. Figure 1a displays the as-cast microstructure of the Al-20% alloy without adding Bi. The microstructure is predominantly composed of unevenly distributed, large-sized coarse rod-like eutectic silicon, with an average contour size ranging from 50 to 120 μm.

Figures 1b–d present the as-cast microstructures of alloys with the addition of 1.0 % Bi, 2.0 % Bi, and 3.0 % Bi, respectively. The complex skeleton arrangement is mainly formed by lamellar Si, as also described by Farahany et al. [14]; Bi has surface activity, which can reduce the surface tension of Al alloys. By reducing the liquid surface tension within the eutectic phase (the layered structure of Al and Si), Bi can reduce the contact angle between Al and Si, making it easier for Al to wet Si particles and encapsulate Si growth peaks, thereby limiting their growth. As seen in Fig. 1, with increased Bi content, the average size of the eutectic silicon structure decreases. The morphology transitions from coarse rod-like structures to finer, short rod-like structures, gradually rounding the angles. When the Bi content reaches 4.0 % (Fig. 1e), the eutectic silicon structure is fully refined, exhibiting a densely distributed worm-like morphology. After increasing the Bi content to 5.0 % (Fig. 1f), there are no significant changes in the distribution and mor-

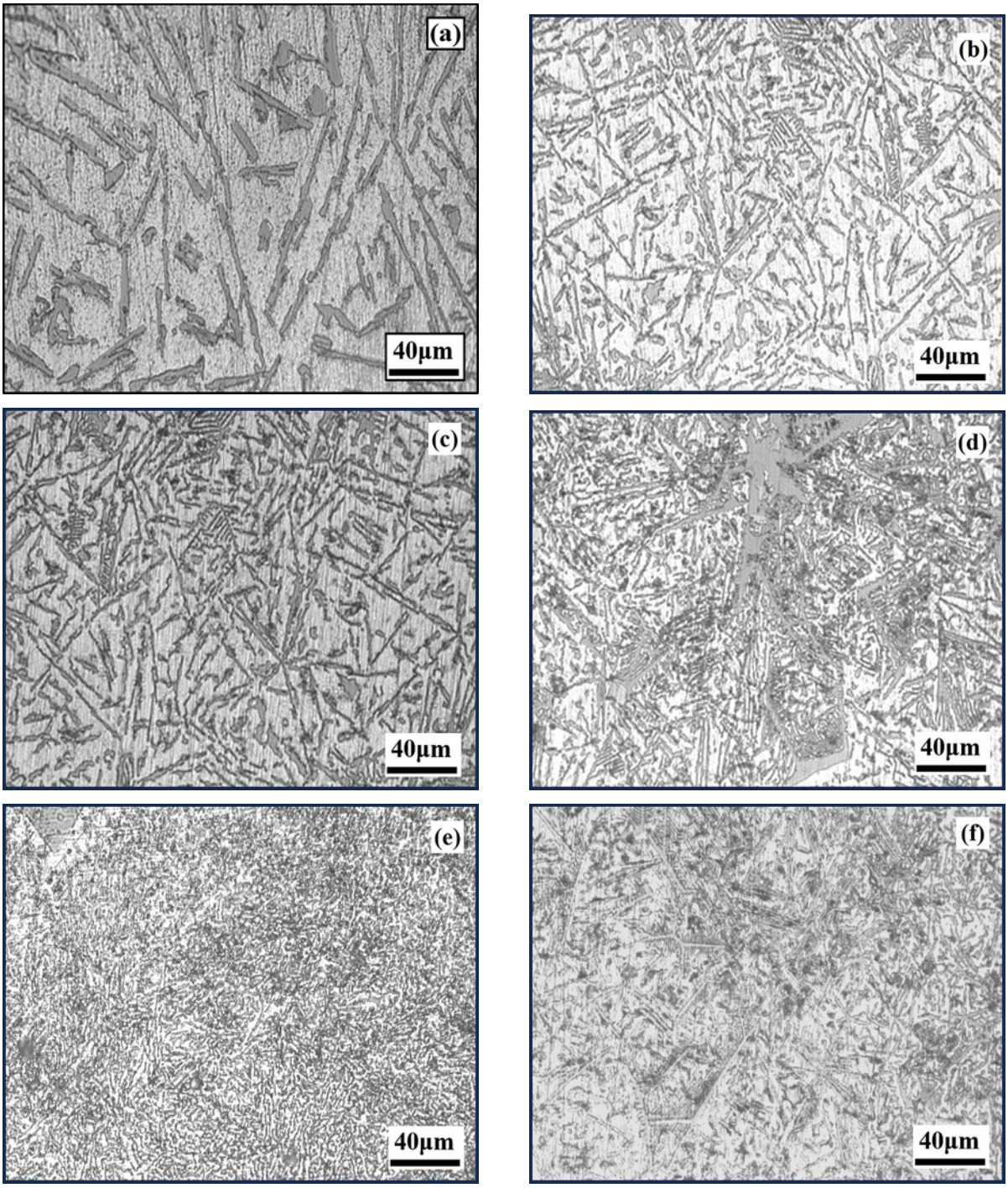

Fig. 1. Optical microstructure of $(Al_{0.8}Si_{0.2})_{100-x}Bi_x$ alloy: (a) $x = 0$ at.%, (b) $x = 1$ at.%, (c) $x = 2$ at.%, (d) $x = 3$ at.%, (e) $x = 4$ at.%, and (f) $x = 5$ at.%.

phology of the eutectic silicon structure compared to Fig. 1e. The microstructure of the eutectic silicon in the as-cast alloy evolves from coarse rod-like structures to finer short rod-like structures and ultimately to a dense worm-like structure.

The presence of Bi leads to a reduction in the crystallization undercooling and the adsorption of Bi atoms at the silicon growth interface, resulting in the formation of multiple twinned crystals. This inhibits the preferred growth orientation of the eutectic silicon. The incorporation of Bi replaces the conventional polyhedral structure and modifies the primary Si structure into a complex crystal with intersecting spines, approximately at a 90-degree angle to the Si angles [17, 18]; Bi mainly accumulates at the ends and edges of the eutectic silicon and primary silicon, par-

ticularly at the angles between silicon dendrites and at the turning points. This increased enrichment or segregation of the Bi phase promotes necking in these regions, leading to the spheroidization of the silicon phase [19]. Higher Bi content results in more nucleation sites and grain boundaries, leading to a decrease in crystal size and a change in morphology. The presence of Bi inhibits the growth rate of the eutectic silicon crystals. This is because Bi interacts with silicon to form compounds or solid solutions with high interfacial energy, thereby hindering crystal growth. The difference in interfacial energy between Bi and Si and the segregation effect of Bi also influence the morphology and distribution of the eutectic silicon. As the Bi content increases, the difference in interfacial energy decreases, resulting in a transition of the eutectic silicon morphology from coarse rod-like structures to finer short rod-like structures, ultimately forming a densely distributed worm-like structure. The addition of Bi may also alter the composition distribution in the alloy, thereby influencing the morphology and distribution of the eutectic silicon. The optimal refinement effect of the eutectic silicon is achieved at a Bi content of 4 %. This is because the synergistic effects of the aforementioned factors reach an optimal state, resulting in the most desirable morphology and distribution of the eutectic silicon.

3.2. Thermophysical property characterization

The DSC curves for $(Al_{0.8}Si_{0.2})_{100-x}Bi_x$ (x = 1, 2, 3, 4, and 5 at.%) alloys are displayed in Fig. 2a. As can be seen, the phase transition temperatures decrease with increasing Bi content. The exothermic peaks during heating can be observed for all alloys, and the phase transition temperatures are in the range of 500–600 ℃ (Fig. 2a). These high phase transition temperatures confer such alloys great potential for high-temperature thermal energy storage applications [20]. The addition of Bi was for tuning phase transition temperatures to satisfy the desired operating temperatures of different applications. The forward and reverse phase transition start and finish temperatures, T_s, T_f, and T_P, were determined from the DSC curves (Fig. 2b) using the tangent method. The phase transition temperatures decrease with increasing Bi content. The T_f for x = 0 is 629 ℃ and that for x = 5 is 517 ℃. This shows that the phase transition temperatures can be tuned over a broad temperature range by composition variation.

The density of $(Al_{0.8}Si_{0.2})_{100-x}Bi_x$ (x = 1, 2, 3, 4, and 5 at.%) alloys is displayed as a function of Bi content in Fig. 2c. It increases slightly with increasing Bi content owing to the addition of the high-density Bi (9.80 g cm^{-3}), which is in the range of 7.21–7.27 g cm^{-3} and much higher than that of organic, inorganic salt and hydrated salt PCMs [21–23]. The large latent heat of phase transition and the high density give rise to a large volumetric thermal energy storage capacity. It was found that the microstructure and phase transition temperature range of alloys undergo a critical transition when x = 4 at.%. Therefore, the properties of $(Al_{0.8}Si_{0.2})_{96}Bi_4$ alloy will be analyzed separately below.

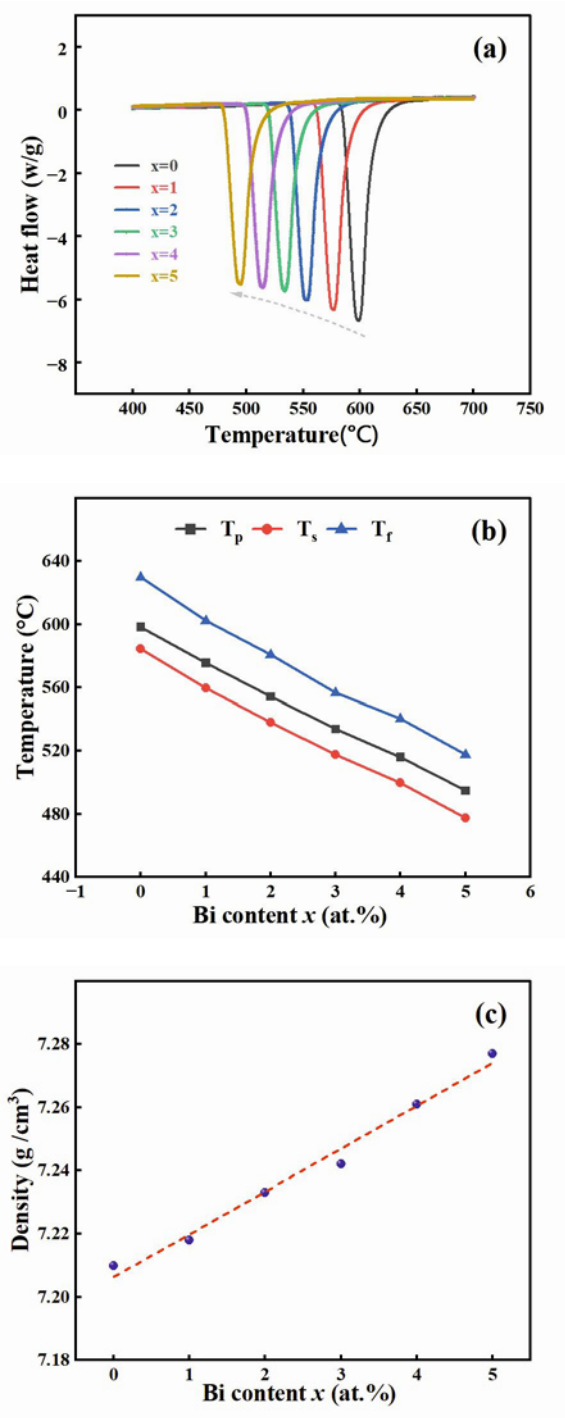

Fig. 2. Calorimetric results for the $(Al_{0.8}Si_{0.2})_{100-x}Bi_x$ alloys (x = 1, 2, 3, 4, and 5 at.%): (a) DSC curves, (b) phase transition temperatures, and (c) density.

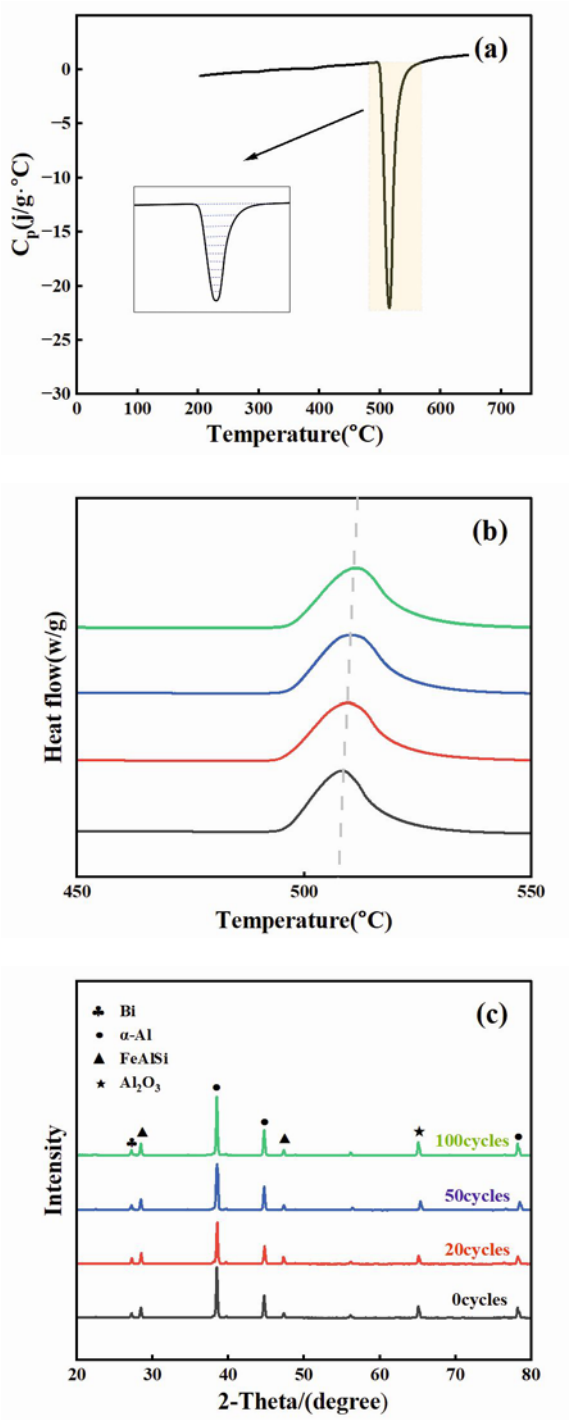

Fig. 3. Thermal cycling stability of phase transition and thermophysical properties for $(Al_{0.8}Si_{0.2})_{96}Bi_4$ alloy: (a) integral plot of enthalpy change calculation, (b) DSC curves measured during the 0–20th, 50th, and 100th thermal cycles across phase transition, and (c) XRD pattern after thermal cycling.

The heat absorbed during the phase transition of the $(Al_{0.8}Si_{0.2})_{96}Bi_4$ alloy is known as the enthalpy of fusion. The enthalpy change was obtained by integrating the area of the exothermic and endothermic peaks on the DSC curves (Fig. 3a). Calculations show that the phase transition enthalpy is 384.6 J g^{-1}. Compared to Al-20Si alloy (phase transition enthalpy of 375–394 J g^{-1} [13]), the $(Al_{0.8}Si_{0.2})_{96}Bi_4$ alloy results in a narrowed phase transition range and a 16.3 % reduction in the phase transition enthalpy.

Figure 3b presents the DSC and peak trend curves of the $(Al_{0.8}Si_{0.2})_{96}Bi_4$ alloy after different thermal cycling cycles. The DSC curve trends after 0, 20, 50, and 100 thermal cycles are nearly identical, with peaks around 514 ℃. This indicates that with an increasing number of cycles, the phase transition temperature of the alloy does not show significant variation. However, as the number of thermal cycles increases, the temperature range in which the peak appears gradually shifts to the right. According to the data in Table 2, after 20, 50, and 100 thermal cycles, the peak temperature of the alloy's phase transition increases by 0.36, 0.56, and 0.70 %, respectively. The phase transition enthalpy decreases from the initial value of –397 to –392.0 J g^{-1}, further decreasing to –384.6 J g^{-1}, and ultimately reaching –379.7 J g^{-1}, corresponding to reductions of 1.3, 3.2, and 4.4 %, respectively. After undergoing 100 cycles of high-temperature thermal cycling, the peak temperature gradually increases with a growth rate of 1 %.

Adding Bi narrows the phase transition temperature range of the $(Al_{0.8}Si_{0.2})_{96}Bi_4$ alloy. This is attributed to modifying the crystal structure or atomic interactions by incorporating Bi, resulting in a reduced energy requirement during the phase transition process. After multiple thermal cycles, the phase transition temperature of the alloy remains relatively unchanged, but the peak temperature gradually increases. This indicates that the thermal cycling process induces subtle changes in the crystal structure, leading to a slight elevation of the peak temperature. It is generally believed that the melting temperature is associated with the interfaces within the crystal structure. The atomic free energy at the interfaces is usually higher, resulting in lower thermodynamic stability during the melting process and promoting heterogeneous nucleation [24]. Melting may initiate from the interfaces, such as grain boundaries, and thus, the more interfaces present, the lower the energy barrier, leading to a lower melting temperature. Typically, interfaces decrease with an increasing number of cycles, implying that the melting point temperature may increase with an increasing number of cycles, explaining the evolution of the melting point temperature in the $(Al_{0.8}Si_{0.2})_{96}Bi_4$ alloy. Zhao et al. [25] observed an increase in phase transition temperature and a decrease in phase transition enthalpy with an increasing number of cycles in their investigation of the thermal stability of Al-7Si alloy. Rudolph et al. [26] found that the increase in melting point temperature could

Table 2. $(Al_{0.8}Si_{0.2})_{96}Bi_4$ DSC data after different thermal cycling heat

Cycle-index	T_s (℃)	T_f (℃)	T_p (℃)	ΔH (J g^{-1})
0 cycles	498.0	554.3	516.1	–397.3
20 cycles	498.3	555.2	518.1	–392.0
50 cycles	498.5	556.8	519.3	–384.6
100 cycles	498.8	567.1	520.1	–379.7

be attributed to the reduction of crystal defects after thermal cycling, leading to an increase in the nucleation energy barrier for crystal melting. The changes in these defects result in an increase in the energy required during the phase transition, thus raising the melting point temperature. The enthalpy is related to entropy change, which typically decreases and stabilizes due to energy dissipation caused by thermal stresses, interfaces, defects, grain orientation, etc. This is consistent with the variation in latent heat observed in the $(Al_{0.8}Si_{0.2})_{96}Bi_4$ alloy.

Figure 3c presents the XRD patterns of $(Al_{0.8}Si_{0.2})_{96}Bi_4$ alloy after different thermal cycling. The XRD reveals the presence of multiple crystalline phases, including the α-Al phase, AlFeSi phase, Al_2O_3 phase, and elemental Bi phase. The formation of the AlFeSi phase, which arises from the interaction between iron, silicon, and aluminum in the original alloy, remains stable after thermal cycling. The presence of oxygen or oxidation on the alloy surface during the thermal cycling process results in forming the Al_2O_3 phase. The presence of Bi is attributed to the lack of compound formation with other elements during the thermal cycling process. These different crystalline phases result from the combined influence of alloy composition, interaction during thermal cycling, and oxidation state of the material. The absence of the Si phase is attributed to the non-equilibrium heat flow conditions in the experiment [27]. The phase composition of the alloy samples does not undergo significant changes after different cycles of thermal cycling; only differences in peak intensities are observed. This indicates that the structure of the $(Al_{0.8}Si_{0.2})_{96}Bi_4$ alloy remains largely unchanged after 100 cycles of high-temperature thermal cycling near the melting point.

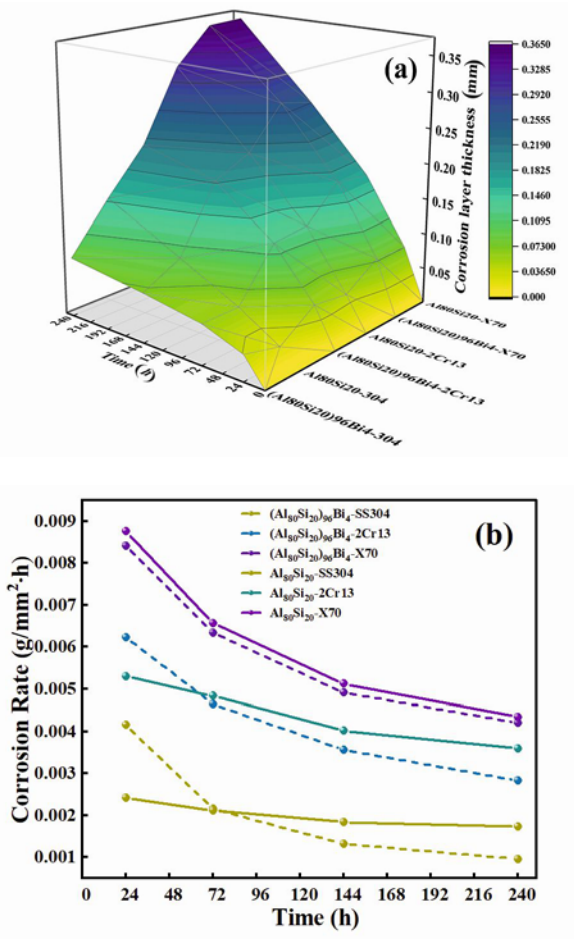

Fig. 4. Corrosion trend diagram between container materials of SS304, 2Cr13, X70 and energy storage alloys of $Al_{80}Si_{20}$ and $(Al_{0.8}Si_{0.2})_{96}Bi_4$: (a) three-dimensional plots of corrosion time and corrosion layer thickness at 560 ℃ and (b) corrosion time and corrosion rate curves.

3.3. Compatibility experiments

Figure 4a depicts three-dimensional plots of corrosion time and corrosion layer thickness for various container materials in different energy storage media at 560 ℃ high-temperature conditions. As shown in Fig. 4a, the corrosion layer thickness of the container materials increases with the corrosion time in different energy storage medium environments. After corrosion for 72 h, the color change in the corrosion layer thickness of 2Cr13 and SS304 tends to stabilize, indicating that their corrosion layer thickness becomes relatively constant. Significant differences exist in the corrosion resistance performance of three container materials in the same energy storage medium. X70 steel shows the maximum increase in corrosion layer thickness after 240 h of corrosion, while the performance of SS304 steel is relatively outstanding. The corrosion behavior of the same container material also varies in different energy storage media. The increase

in corrosion layer thickness when in contact with the $Al_{80}Si_{20}$ energy storage medium is significantly higher than when in contact with the $(Al_{80}Si_{20})_{96}Bi_4$ energy storage medium.

Figure 4b presents corrosion time and corrosion rate curves for different container materials in contact with different energy storage media. With the increasing corrosion time, the corrosion rates between all container materials and energy storage media tend to decrease. The corrosion rate curves of the 2Cr13 and SS304 container materials gradually level off with time. X70 steel exhibits a higher corrosion rate, while SS304 steel has the lowest corrosion rate. The corrosion rate of the $(Al_{80}Si_{20})_{96}Bi_4$ is slightly lower than that of the $Al_{80}Si_{20}$, suggesting that the $(Al_{80}Si_{20})_{96}Bi_4$ exhibits enhanced compatibility with SS304.

Figure 5a shows the cross-sectional SEM image of SS304 in contact with $(Al_{0.8}Si_{0.2})_{96}Bi_4$ after static exposure at 560 ℃ for 240 h. In our study, we employed standard scanning electron microscopy (SEM) techniques for microstructural analysis. While backscattered electron imaging was not utilized, the applied SEM methods provided sufficient resolution to observe the pertinent microstructural features, especially regarding the influence of bismuth on grain size and phase composition. The alloy melt has penetrated the surface of SS304, with a penetration depth of approximately 50 µm. There is partial bonding between the SS304 substrate and the alloy melt. From Fig. 5c, a transitional layer exists at the contact interface between the SS304 substrate and the alloy melt. Combined with EDS mapping, the transitional layer is composed of two phases: a bright white phase rich in Al and a dark black phase rich in Fe.

Due to the excellent wetting ability of Al atoms on the surface of Fe-based metals and the low heat of formation of $FeAl_3$ in Al-Fe compounds, the $FeAl_3$ phase is initially formed at the contact interface between the $(Al_{0.8}Si_{0.2})_{96}Bi_4$ alloy melt and the Fe-based material. With increasing time and infiltration of Al melt, a concentration gradient exists in the transitional layer. Therefore, the newly formed $FeAl_3$ phase gradually diffuses and accumulates towards the interior of the alloy melt. Due to the different crystal structures between intermetallic compounds and metals, under the influence of microstructural transformation stresses [28], the newly formed $FeAl_3$ phase on the surface of the SS304 substrate partially flakes off and dissolves, exposing fresh substrate, which then recontacts with the Al melt to form intermetallic compounds. This process repeats continuously, allowing for mutual infiltration and fusion of the two phases. Similar phenomena have also been observed by Heumann et al. [29] in the study of the interfacial layer formation mechanism during the hot-dip aluminization of steel. When liquid Al comes into contact with solid steel, mutual diffusion

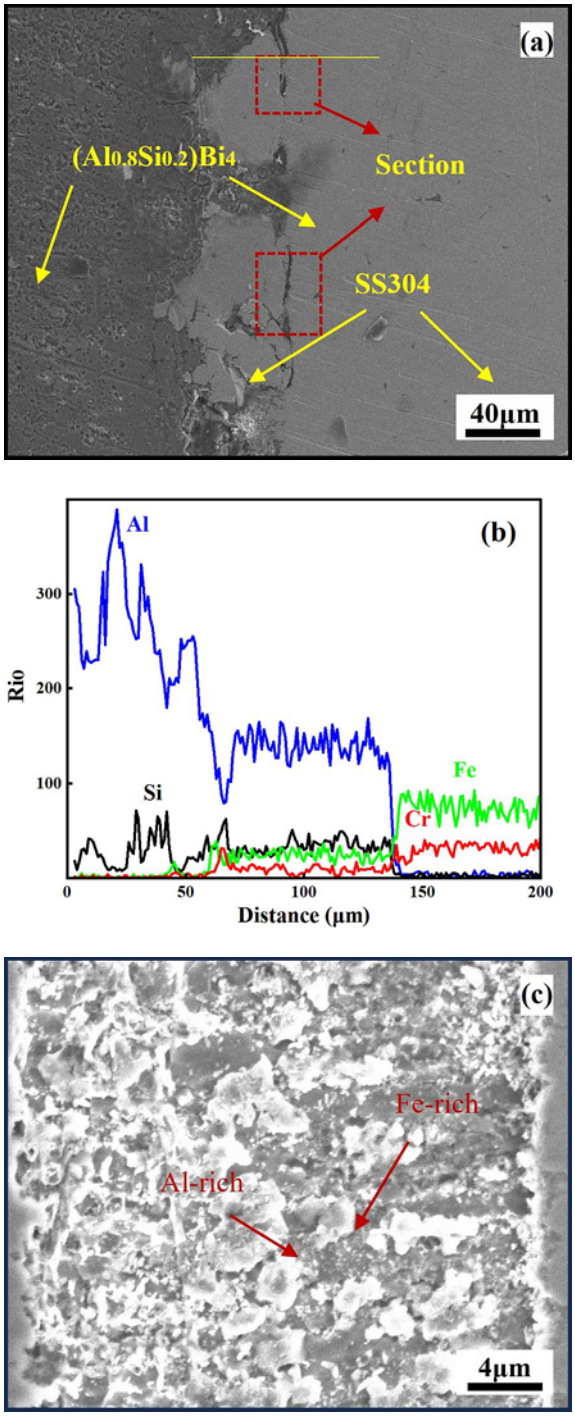

Fig. 5. Static reaction experiment cross-section of SS304 in $(Al_{0.8}Si_{0.2})_{96}Bi_4$ at 560 ℃ for 240 h: (a) labeled SEM image; (b) EDS line scan results, and (c) SEM image.

of Al and Fe atoms occurs at the interface, forming the $FeAl_3$ phase. Due to concentration fluctuations, a small region within the $FeAl_3$ layer with a concentration equivalent to the Fe_2Al_5 phase is formed, and recrystallization of the phase starts from the surface of the $FeAl_3$ phase, promoting the growth of Fe_2Al_5 in the diffusion direction.

Al melt and Fe corrosion is mainly diffusion corrosion [30], also known as AlFe co-diffusion corrosion. Therefore, the growth of the corrosion layer thickness follows a parabolic law. During the corrosion process, the presence of Cr and Ni elements in the container materials, 2Cr13 and SS304, plays a crucial role. Initially, the Cr and Ni elements undergo oxidation, forming a protective Cr_2O_3 film. Subsequently, they react with NiO to generate a dense spinel structure known as $NiCr_2O_4$ [31–35]. This compact lattice structure effectively impedes the diffusion of Al atoms into the steel matrix, thereby reducing the thickness of the corrosion layer and lowering the corrosion rate. Conversely, X70, which lacks these elements, experiences a faster growth of the corrosion layer, primarily composed of AlFe co-diffusion layers. Furthermore, adding Bi refines the grain structure of $(Al_{80}Si_{20})_{96}Bi_4$ energy storage material. Since grain size and the number of grain boundaries are inversely proportional, increasing the number of grain boundaries promotes atomic diffusion [36]. Recent research highlights the influence of grain boundary density on atomic diffusion rates. Xiao et al. [37] found that corrosion rates at polycrystalline grain boundaries in Fe surfaces were significantly faster than in twin and single crystals, indicating a link between increased grain boundaries and accelerated atomic activity. Similarly, Jin et al. [38] observed that grain boundary diffusion in Nd-Fe-B magnets, enhanced by aluminum addition, led to faster diffusion of rare-earth elements, further evidencing the role of grain boundaries in promoting atomic diffusion. Consequently, adding Bi promotes the diffusion of Cr and Ni, facilitating the rapid formation of a dense oxide film. This process effectively retards the occurrence of Al-Fe corrosion, as depicted in Fig. 6. When the Al-based alloy melt comes into initial contact with the container material, it is akin to subjecting the container material to a thermal Al deposition treatment, resulting in the formation of a thin yet dense oxide film. This oxide film exhibits excellent barrier properties, slowing the onset of corrosion and reducing the corrosion rate [39–41]. Therefore, even without Cr elements, X70 exhibits a decreasing trend in corrosion rate with increasing corrosion time, highlighting the efficacy of the formed oxide film. In summary, SS304 steel exhibits relatively enhanced container compatibility, and X70 steel shows deteriorated compatibility due to the absence of the Cr element.

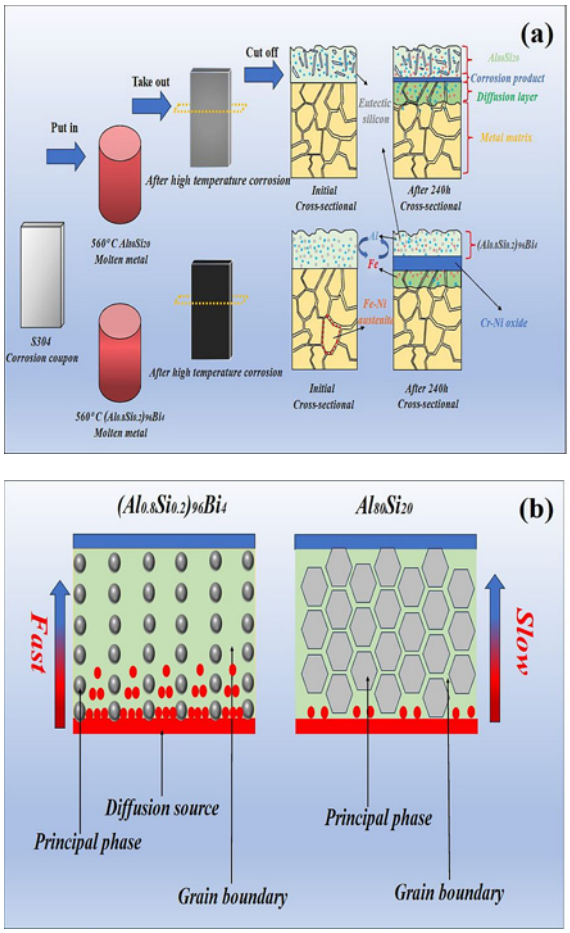

Fig. 6. Microscopic mechanism of diffusion corrosion of SS304 at 560 °C in phase change energy storage alloy melt: (a) corrosion mechanism and (b) microscopic mechanism of the relationship between grain size and atomic diffusion rate.

4. Conclusions

We developed the a (Al0.8Si0.2)96Bi4 phase change energy storage alloy in this study, capitalizing on its high-temperature capabilities. This alloy demonstrates a significant enthalpy change of up to –397 J g^{-1}. Notably, even after 100 high-temperature thermal cycles, its phase composition remains impressively stable. This stability, coupled with the Bi-induced grain size refinement and accelerated Cr and Ni atom migration, contributes to the rapid formation of chromium-nickel oxide on the surface. These properties make the alloy particularly suitable for applications in environments with temperatures ranging between 500–600 ℃.

Acknowledgements

This research was supported by the Natural Science Foundation of Heilongjiang Province (LH2023E016), the Hainan Province Science and Technology Special Fund (ZDYF2023090), and the Youth Science Fund and Research Startup Fund of Northeast Petroleum University (2020QNL-06).

References

[1] C. R. Matos, J. F. Carneiro, P. P. Silva, Overview of large-scale underground energy storage technologies for integration of renewable energies and criteria for reservoir identification, J. Energy Storage 210 (2019) 41–258. https://doi.org/10.1016/j.est.2018.11.023

[2] A. Rawson, C. Villada, M. Kolbe, V. Stahl, F. Kargl, Suitability of aluminum copper silicon eutectic as a phase change material for thermal storage applications: Thermophysical properties and compatibility, J. Energy Storage 4 (2022) e299. https://doi.org/10.1002/est2.299

[3] Z. Sun, L. Zou, X. Cheng, J. Zhu, Y. Li, W. Zhou, Fabrication, structure, and thermal properties of Mg-Cu alloys as high-temperature PCM for thermal energy storage, Materials 14 (2021) 4246. https://doi.org/10.3390/ma14154246

[4] M. Zha, H. M. Zhang, X. T. Meng, H.-L. Jia, S.-B. Jin, G. Sha, H. Y. Wang, Y. J. Li, H. J. Roven, Stabilizing a severely deformed Al-7Mg alloy with a multimodal grain structure via Mg solute segregation, J. Mater. Sci. & Technol. 89 (2021) 141–149. https://doi.org/10.1016/j.jmst.2021.01.086

[5] Z. Wang, H. Wang, X. Li, D. Wang, Q. Zhang, G. Chen, Z. Ren, Aluminum and silicon based phase change materials for high capacity applied thermal engineering, Therm. Eng. 89 (2015) 204–208. https://doi.org/10.1016/j.applthermaleng.2015.05.037

[6] Z. Wang, H. Wang, M. Yang, W. Sun, G. Yin, Q. Zhang, Z. Ren, Thermal reliability of Al-Si eutectic alloy for thermal energy storage, Mater. Res. Bull. 95 (2017) 300–306. https://doi.org/10.1016/j.materresbull.2017.07.040

[7] X. Zhang, W. Chen, Review on corrosion-wear resistance performance of materials in molten aluminum and its alloys, Trans. Nonferrous Met. Soc. China 25 (2015) 1715–1731. https://doi.org/10.1016/S1003-6326(15)63777-3

[8] M.-A. Van Ende, M. Guo, J. Proost, B. Blanpain, P. Wollants, Interfacial reactions between oxygen containing Fe and Al at the onset of liquid Fe deoxidation by Al addition, ISIJ Int. 50 (2010) 1552–1559. https://doi.org/10.2355/isijinternational.50.1552

[9] H. C. Shih, J. W. Hsu, C. N. Sun, S. C. Chung, The lifetime assessment of hot-dip 5% Al-Zn coatings in chloride environments, Surf. Coat. Technol. 150 (2002) 70–75. https://doi.org/10.1016/S0257-8972(01)01508-0

[10] A. Raffaitin, F. Crabos, E. Andrieu, D. Monceau, Advanced burner-rig test for oxidation-corrosion resistance evaluation of MCrAlY/superalloys systems, Surf. Coat. Technol. 201 (2006) 3829–3835. https://doi.org/10.1016/j.surfcoat.2006.07.256

[11] T. Man, Z. Xiang, L. Zhang, E. Wang, Effect of in situ phases on microstructure and properties in Al-Bi immiscible alloy, Mater. Sci. Technol. 36 (2020) 1250–1256. https://doi.org/10.1080/02670836.2020.1769880

[12] M. Â. O. de Alfaia, R. Oliveira, T. S. Lima, F. E. Mariani, L. C. Casteletti, N. Cheung, A. Garcia, Effects of cooling rate and microstructure scale on wear resistance of unidirectionally solidified Al-3.2wt.%Bi-(1;3) wt.%Pb alloys, Mater. Today Commun. 25 (2020) 101659. https://doi.org/10.1016/j.mtcomm.2020.101659

[13] M. Dias, R. Oliveira, R. Kakitani, N. Cheung, H. Henein, J. E. Spinelli, A. Garcia, Effects of solidification thermal parameters and Bi doping on silicon size, morphology and mechanical properties of Al-15wt.% Si-3.2wt.% Bi and Al-18wt.% Si-3.2wt.% Bi alloys, J. Mater. Res. Technol. 9 (2020) 3460–3470. https://doi.org/10.1016/j.jmrt.2020.01.083

[14] S. Farahany, A. Ourdjini, T. A. A. Bakar, M. H. Idris, On the refinement mechanism of silicon in Al-Si-Cu-Zn alloy with addition of Bi, Metall. Mater. Trans. A 45 (2014) 1085–1088. https://doi.org/10.1007/s11661-013-2158-0

[15] H. Wei, C. Qiu, C. Wang, K. Lin, S. Yang, J. Han, Y. Lu, X. Liu, Development of phase change materials using hydrolyzed Al-Bi composite powder for solar energy storage, Chem. Eng. J. 421 (2021) 127836. https://doi.org/10.1016/j.cej.2020.127836

[16] Z. Yang, D. Y. Cong, X. M. Sun, Z. H. Nie, Y. D. Wang, Enhanced cyclability of elastocaloric effect in boron-microalloyed Ni-Mn-In magnetic shape memory alloys, Acta Mater. 127 (2017) 33–42. https://doi.org/10.1016/j.actamat.2017.01.025

[17] F. Yilmaz, O. A. Atasoy, R. Elliott, Growth structures in aluminium-silicon alloys II. The influence of strontium, J. Crystal Growth 118 (1992) 377–384. https://doi.org/10.1016/0022-0248(92)90086-X

[18] F. Yilmaz, R. Elliott, The microstructure and mechanical properties of unidirectionally solidified AlSi alloys, J. Mater. Sci. 24 (1989) 2065–2070. https://doi.org/10.1007/BF02385422

[19] K. V. Nikitin, V. I. Nikitin, I. Yu. Timoshkin, V. B. Deev, Effect of adding rare-earth and alkaline-earth metals to aluminum-based master alloys on the structure and properties of hypoeutectic silumines, Metallurgist 65 (2021) 681–688. https://doi.org/10.1007/s11015-021-01205-x

[20] F. Jiang, L. Zhang, X. She, C. Li, D. Cang, X. Liu, Y. Xuan, Y. Ding, Skeleton materials for shape-stabilization of high temperature salts based phase change materials: A critical review, Renew. Sustain. Energy Rev. 119 (2020) 109539. https://doi.org/10.1016/j.rser.2019.109539

[21] S. Li, L. He, H. Lu, J. Hao, D. Wang, F. Shen, C. Song, G. Liu, P. Du, Y. Wang, D. Cong, Ultrahigh-performance solid-solid phase change material for efficient, high-temperature thermal energy storage, Acta Mater. 249 (2023) 118852. https://doi.org/10.1016/j.actamat.2023.118852

[22] K. Yu, Y. Liu, Y. Yang, Review on form-stable inorganic hydrated salt phase change materials: Preparation, characterization and effect on the thermophysical properties, Appl. Energy 292 (2021) 116845. https://doi.org/10.1016/j.apenergy.2021.116845

[23] D. G. Atinafu, Y. S. Ok, H. W. Kua, S. Kim, Thermal properties of composite organic Phase Change Materials (PCMs): A critical review on their engineering chemistry, Applied Thermal Engineering 181 (2020) 115960. https://doi:10.1016/j.applthermaleng.2020.115960

[24] H. Van Swygenhoven, Grain boundaries and dislocations, Science 296 (2002) 66–67. https://doi.org/10.1126/science.1071040

[25] Y. Zhao, H. B. Liu, C. Y. Zhao, Experimental study on the cycling stability and corrosive property of Al-Si alloys as phase change materials in high-temperature heat storage, Sol. Energy Mater. Sol. Cells 203 (2019) 110165. https://doi.org/10.1016/j.solmat.2019.110165
[26] P. Rudolph, Fundamentals and engineering of defects, Prog. Crystal Growth Charact. Mater. 62 (2016) 89–110. https://doi.org/10.1016/j.pcrysgrow.2016.04.004
[27] R. V. Reyes, L. C. Casteletti, A. Garcia, J. E. Spinelli, Characterization of microstructure and wear resistance of a monotectic Al-Bi-Zn alloy, J. Phys. Chem. Solids 147 (2020) 109631. https://doi.org/10.1016/j.jpcs.2020.109631
[28] S. Chen, D. Yang, M. Zhang, J. Huang, X. Zhao, Interaction between the growth and dissolution of intermetallic compounds in the interfacial reaction between solid iron and liquid aluminum, Metall. Mater. Trans. A 47 (2016) 5088–5100. https://doi.org/10.1007/s11661-016-3667-4
[29] T. Heumann, S. Dittrich, Über die Kinetik der Reaktion von festem und flüssigem Aluminium mit Eisen, Z. Metallkd. 50 (1959) 617–625 (in German). https://doi.org/10.1515/ijmr-1959-501010
[30] X. Zhang, W. Chen, Review on corrosion-wear resistance performance of materials in molten aluminum and its alloys, Trans. Nonferrous Met. Soc. China 25 (2015) 1715–1731. https://doi.org/10.1016/S1003-6326(15)63777-3
[31] J. Ehlers, D. J. Young, E. J. Smaardijk, A. K. Tyagi, H. J. Penkalla, L. Singheiser, W. J. Quadakkers, Enhanced oxidation of the 9%Cr steel P91 in water vapour containing environments, Corrosion Science 48 (2006) 3428–3454. https://doi.org/10.1016/j.corsci.2006.02.002
[32] C. T. Fujii, R. A. Meussner, Oxide structures produced on iron-chromium alloys by a dissociative mechanism, J. Electrochem. Soc. 110 (1963) 1195. https://doi.org/10.1149/1.2425624
[33] A. Rahmel, Einfluss von Wasserdampf und Kohlendioxyd auf die Oxydation von Eisen in Sauerstoff bei hohen Temperaturen, Corros. Sci. 5 (1965) 815–820 (in German). https://doi.org/10.1016/S0010-938X(65)80011-7
[34] Y. J. Wang, Y. N. Zeng, J. G. Li, Z. Y. Gao, Leaching characteristics and mineralogical control of chromium in electric-arc-furnace stainless-steel slag, Mater. Technol. 55 (2021) 127–133. https://doi.org/10.17222/mit.2020.156
[35] R. Karthikeyan, R. Subbiah, Investigation of the effect of Inconel particulate filler on the mechanical and fire-retardant characteristics of GFRP composites, Mater. Technol. 56 (2022) 653–659. https://doi.org/10.17222/mit.2022.559
[36] Z. Shen, J. Zhang, S. Wu, X. Luo, B. M. Jenkins, M. P. Moody, S. Lozano Perez, X. Zeng, Microstructure understanding of high Cr-Ni austenitic steel corrosion in high-temperature steam, Acta Mater. 226 (2022) 117634. https://doi.org/10.1016/j.actamat.2022.117634
[37] Z. Xiao, Y. Huang, Z. Liu, W. Hu, Q. Wang, C. Hu, The role of grain boundaries in the corrosion process of F surface: Insights from ReaxFF molecular dynamic simulations, Metals 12 (2022) 876. https://dx.doi.org/10.3390/met12050876
[38] Z.-H. Jin, L. Jin, G.-F. Ding, S. Guo, B. Zheng, S.-N. Fan, Z.-X. Wang, X.-D. Fan, J. Zhu, R.-J. Chen, A. Yan, J. Pan, X. Liu, Coercivity enhancement of sintered Nd-Fe-B magnets by grain boundary diffusion with $Pr_{80-x}Al_xCu20$ alloys, Chinese Physics B 32 (2023) 017505. https://dx.doi.org/10.1088/1674-1056/ac6741
[39] R. C. Wolfe, B. A. Shaw, The effect of thermal treatment on the corrosion properties of vapor deposited magnesium alloyed with yttrium, aluminum, titanium, and misch metal, J. Alloys Compd. 437 (2007) 157–164. https://doi.org/10.1016/j.jallcom.2006.07.111
[40] W. Jiang, Z. Fan, G. Li, X. Liu, F. Liu, Effects of hot-dip galvanizing and aluminizing on interfacial microstructures and mechanical properties of aluminum/iron bimetallic composites, J. Alloys Compd. 68 (2016) 742–751. https://doi.org/10.1016/j.jallcom.2016.07.085
[41] M. Vončina, A. Nagode, J. Medved, T. Balaško, Influence of temperature on interaction kinetics between molten aluminium alloy Al99.7 and tool steel H11, Mater. Technol. 57 (2023) 401–405. https://doi.org/10.17222/mit.2023.825